ELSEVIER

Contents lists available at ScienceDirect

Tectonophysics

journal homepage: www.elsevier.com/locate/tecto



Synorogenic extension and extrusion in southern Taiwan

Wei-Hao Hsu^a, Timothy B. Byrne^b, Jonathan C. Lewis^c, Yue-Gau Chen^{a,d,*}, Po-Yi Yeh^a

- ^a Department of Geosciences, National Taiwan University, No. 1, Sec. 4, Roosevelt Road, Taipei 106, Taiwan
- b Department of Geosciences, University of Connecticut, Storrs, CT 06269-1045, United States and Department of Natural Resources and Environmental Studies, National Dong Hwa University, Hualien, Taiwan
- ^c Geoscience, Indiana University of Pennsylvania, 302 E. Walk, Indiana, PA 15705, United States
- ^d Research Center for Environmental Changes, Academia Sinica, No. 128, Sec. 2, Academia Road, Taipei 115, Taiwan

ARTICLE INFO

Keywords: Taiwan Synorogenic extension Extrusion Paleostress inversion

ABSTRACT

Paleostress inversion of 141 outcrop-scale faults across the eastern flank of the southern Central Range of Taiwan where leveling and GPS data suggest a steep gradient in rock uplift rates yields two main kinematic phases of deformation. Phase 1 consists of 93 normal faults that generally dip moderately northeast whereas phase 2 consists of 48 strike-slip faults that generally dip steeply west-northwest. Both phases record NE-trending subhorizontal extension but different orientations of principal shortening; in phase 1, the principal shortening axis is nearly vertical whereas in phase 2 it plunges gently to moderately southeast. The northeast extension is consistent with extension directions obtained from GPS and earthquake focal mechanisms in the central part of the southern Central Range. However, these indicators of contemporary deformation also reveal more complicated states of stress along the eastern and western flanks of the range and in the deep crust southwest of the range. We interpret these more complicated stress states as reflecting "forceful extrusion" of the southern Central Range where the lower crust is being pinched between more rigid crustal blocks represented by the Peikang High and the Luzon Arc. In this context, the temporal progress from strike-slip to normal faulting observed in outcrops may reflect the advection of the rocks from lower to higher structural levels. The northeast extension normal faults can be interpreted that accommodating the lateral and vertical movement of the crust in the southern Central Range. Based on thermochronological data and the onset of extrusion in southwest Taiwan in the late Pleistocene, we infer that this SW extrusion process may be younger the 0.5 Ma.

1. Introduction

Extensional deformation is common in the hinterlands of many contractional orogenic belts, such as the Basin and Range Province in the cordillera of western North America (Bennett et al., 2003; Coney and Harms, 1984; Thatcher et al., 1999), Variscan crust in Frence (Malavieille et al., 1990), Tibet (Armijo et al., 1986; Chevalier et al., 2020; Molnar and Lyon-Caent, 1989; Yin et al., 1999), and Andes (Dalmayrac and Molnar, 1981; Suarez et al., 1983; Tibaldi and Bonali, 2018). These orogenic hinterlands are characterized by high topography and thickened crust, marked by synorogenic extensional structures at high elevations or on steep topographic slopes. In contrast contractional structures occur at lower elevations on the flanks of the mountain belts. In many cases, the extension is perpendicular to the orogen (Bennett et al., 2003; Dalmayrac and Molnar, 1981; Suarez et al., 1983; Thatcher et al., 1999; Tibaldi and Bonali, 2018) or parallel to the orogen (Armijo

et al., 1986; Chevalier et al., 2020; Molnar and Lyon-Caent, 1989; Yin et al., 1999). In Taiwan, although mountain heights are lower than in these classic orogens, GPS-derived strain rate data and earthquake focal mechanisms show that the high elevations are dominated by extension, whereas the lower elevations are dominated by contraction (Hsu et al., 2009; Wu et al., 2008). This phenomenon is similar to the orogenic belts in Tibet and Andes. Previous studies proposed different hypothesis to explain the extension in the Central Range, including buoyancy forces related to subducted continental crust (Lin, 2000), and gravitational collapse of over-thickened continental crust (Hsu et al., 2009), possibly associated with underplating (Crespi et al., 1996). These hypotheses provide a mechanism for vertical shortening and gravitational collapse of the upper crust in the Central Range, but not the relatively unusual extension direction, which is oblique to the orogen rather than orthogonal. This important observation suggests a more complicated gravitational model or tectonic process may be responsible for extension in the

^{*} Corresponding author at: Research Center for Environmental Changes, Academia Sinica, No. 128, Sec. 2, Academia Road, Taipei 115, Taiwan. E-mail address: ygchen@gate.sinica.edu.tw (Y.-G. Chen).

core of the southern Central Range. Moreover, the structures that accommodate the relatively high rates of rock uplift (Ching et al., 2011; Hsu et al., 2018) and exhumation (Hsu et al., 2016) in the southern Central Range are still unknown.

In this paper, we document late-stage structures exposed along the eastern flank of the southern Central Range where leveling and GPS data suggest a steep gradient in uplift rates and we integrate these data with earthquake focal mechanism to evaluate different hypotheses for the origin of synorogenic normal faults. We propose a tectonic model in which the crust in southwest Taiwan is shortened between the obliquely colliding Peikang High and the Luzon Arc and that shortening is accommodated by lateral and vertical movement of the crust.

2. Tectonic and geologic background

The Taiwan orogenic belt is located on the boundary between the Philippine Sea and Eurasian Plates (Fig. 1A). The Philippine Sea plate is subducting beneath the Eurasian Plate along the Ryukyu Trench in the north, whereas to the south of Taiwan, the Philippine Sea plate is overriding the crust of the South China Sea along the Manila trench (Teng, 1990). With the northwestward movement of the Philippine Sea Plate at 82 mm per year (Yu et al., 1997) since 5 Ma (Ho, 1986; Teng, 1990), resulting in an oblique collision between the north trending Luzon arc and the northeast trending passive continental margin of the Eurasia plate (Chai, 1972). The Taiwan mountain belt can be divided into seven tectonostratigraphic units, from east to west are the Coastal Range, the Longitudinal Valley, the Tananao Metamorphic Complex

(Tailuko and Yuli belts), the Backbone Range slate belt, the Hsüehshan Range slate belt, the Western Foothill fold and thrust belt, and Coastal plain (Fig. 1A)(Ho, 1988). Across the orogeny, there is an overall eastward increase in the metamorphic grade and complexity of deformation (Beyssac et al., 2007; Chen, 1994). From west to east in the Central Range, the dominant foliation (S1) is overprinted by a crenulation cleavage (S2) (Clark et al., 1992; Stanley et al., 1981). There is also a general change in the dip direction of both S1 and S2; in the west the dominant foliation dips east whereas in the east the dominant foliation dips west. This fan-shaped pattern of foliation has been interpreted to reflect east vergent backfolding (Faure et al., 1991; Fisher et al., 2007; Stanley et al., 1981), or alternatively as a result of motion along an east-dipping, normal fault zone (Crespi et al., 1996).

The western margin of the Taiwan orogenic belt shows a stretched S shape in map view (Fig. 1A). This shape represents the influence of a pre-Tertiary basement feature, the Peikang High, in the subducting plate (Fig. 1A). The trend of folds and faults (Angelier et al., 1986), and GPS data (Bos et al., 2003; Chang et al., 2003) surrounding the Peikang High reveal a fan-shaped pattern of compressive axes in the fold and thrust belt (Fig. 1A). This pattern suggests the Peikang High acts as a rigid indenter (Hu et al., 1996), deflecting the fold and thrust belt but not the Backbone Range slate belt and Tailuko Belt.

Vertical GPS and leveling data in southern Taiwan show an eastward increasing uplift rate from Western Foothills to the topographic divide, and then a decreasing uplift rate along the eastern flank of the southern Central Range (Fig. 1C; Ching et al., 2011; Hsu et al., 2018). This pattern is similar to the topographic profile in southern Taiwan (Fig. 1C).

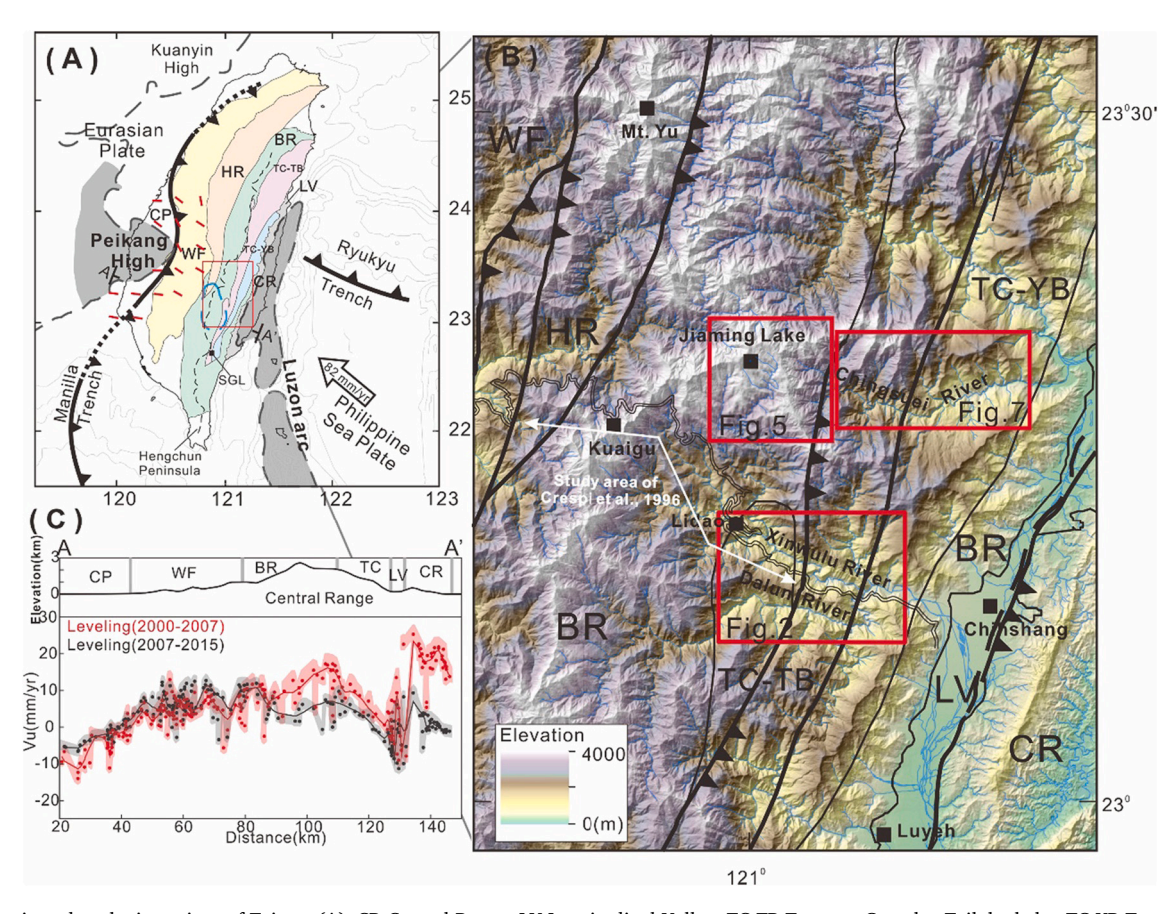


Fig. 1. Tectonic and geologic settings of Taiwan (A). CR-Coastal Range; LV-Longitudinal Valley; TC-TB-Tananao Complex-Tailuko belts; TC-YB-Tananao Complex-Yuli Belt; BR-Backbone Range slate belt; HR-Hsüehshan Range slate belt; WF-Western Foothills; CP-Coastal Plain. Short red line represents the direction of the compressive axes from GPS (Bos et al., 2003); Blue dash line represents the tremors from Chen et al. (2018); Black dash line represents the topographic divide (ridge crest); SGL-Small Ghost Lake. (B) Topography and geologic settings of the study area. Geology from Chen (2000); thick black line represents the fault; red box shows the field area; enlarged in Figs. 2, 5 and 7. (C) Topographic profile and leveling data from Hsu et al., 2018 (A-A'). (For interpretation of the references to colour in this figure legend, the reader is referred to the web version of this article.)

However, leveling profiles across southern Taiwan during two different time periods show a significant gradient but different rate of uplift along the eastern flank of the Central Range; the maximum uplift rate is 17.19 mm/yr. (Ching et al., 2011) from 2000 to 2008, and 10 mm/yr from 2007 to 2015 (Hsu et al., 2018), respectively (Fig. 1C). Hsu et al. (2018) point out that Ching et al. (2011) corrected the coseismic deformation of the 1999 Mw 7.6 Chi-Chi and 2003 Mw 6.8 Chengkung earthquakes but did not correct the post-seismic deformation, resulting in the discrepancy of the uplift rate in the eastern flank of the Central Range between two time periods. The mean uplift rate of 6 mm/yr between the eastern Central Range and the frontal fold and thrust belt (Hsu et al., 2018).

The strain-rate field estimated from GPS data exhibits a contraction regime in the Coastal Range and western Taiwan, whereas significant extension in northeastern Taiwan and Central Range (Bos et al., 2003; Chen et al., 2017; Hsu et al., 2009). GPS and geologic data have previously demonstrated a deflection of contraction axes in western Taiwan from east-west trends to northeast-southwest trends (Fig. 1A; Angelier et al., 1986; Bos et al., 2003; Chang et al., 2003; Chen et al., 2017; Hsu et al., 2009). Geologic (Angelier et al., 2009; Lacombe et al., 2001) and geodetic (Bos et al., 2003; Hu et al., 2007; Lacombe et al., 2001) data also suggest lateral extrusion in southwestern Taiwan which is consistent with sandbox experiments of an oblique collision (Lu and Malavieille, 1994). The fan-shaped contraction axes and southwest lateral extrusion are interpreted to be due to the relatively rigid Peikang High colliding against the Luzon Arc (Fig. 1A; Hu et al., 1996). Quaternary paleostress analyses also suggest the southwest lateral extrusion in southwestern Taiwan during the late Pleistocene (Lacombe et al., 2001).

The distribution of earthquake focal mechanisms show a correlation with topography in Taiwan, with high elevation (elevation >1500 m) dominated by normal and strike-slip faulting, whereas the surrounding lower elevations are dominated by thrust and strike-slip faulting (Chen et al., 2017; Hsu et al., 2009; Wu et al., 2008). The stress field derived from earthquake focal mechanisms shows that σ_1 has a fan-shaped pattern in western Taiwan, which is in agreement with previous studies based on geological data (Angelier et al., 1986), borehole breakout data (Suppe et al., 1985), and the contraction axes derived from GPS velocity field (Bos et al., 2003; Chang et al., 2003; Chen et al., 2017; Hsu et al., 2009). These observations imply a brittle deformation regime against the Peikang High and a consistent deformation pattern from the surface down to a maximal depth of 20 km (Chen et al., 2017). In addition, the upper crust of the southern Central Range is dominated by normal faulting with northeast-southwest extension (Conand et al., 2020; Crespi et al., 1996; Hsu et al., 2009; Wu et al., 2008). Previous studies suggest the extension in the southern Central Range could be due to buoyancy forces related to subducted continental crust (Lin, 2000), or to gravitational collapse resulting from over-thickened continental crust (Hsu et al., 2009), or possibly associated with underplating at depth (Crespi et al., 1996), or left-lateral transtensional brittle deformation (Conand et al., 2020).

In the northern part of the southern Central Range a zone of low seismicity and high heat flow correlates with a crustal-scale zone of ambient tremors, suggesting ductile flow of the crust in this area (Fig. 1A). The tremors form a sub-vertical, southeast dipping ellipsoidal structure (Chuang et al., 2014; Lai et al., 2012) and Ide et al. (2015) proposed that the tremors reflected WNW-ESE compression. In the upper crust, above the tremor cluster, swarms of small earthquakes, typically with normal fault focal mechanisms, delineate sub-vertical planar structures (Chuang et al., 2014). Chen et al. (2018) argued that as the Eurasian continental crust is progressively subducted both ambient temperature and the resistance to subduction increase, leading to the release of metamorphic fluids and the development a sub-vertical, brittle-ductile shear zone. Recent helium isotope studies of well and hot spring waters structurally above the tremors also indicate mantle contamination which may signal the possible existence of melt in the lower crust and upper mantle in the southern Central Range (Chen et al., 2019). The correlation of high helium isotopic ratios with deep tremors and shallow extensional structures suggests that the tremors represent crustal-scale conduits that allow the helium movement through from the upper mantle (Chen et al., 2019).

Recent fission track and (U—Th)/He dates of totally reset detrital apatite and zircon grains indicate an accelerated exhumation in the eastern Central Range of the Taiwan orogenic belt from 2 to 1.5 Ma (Hsu et al., 2016). The age-elevation curves and thermal models imply three stages of exhumation: prior to ca. 2 Ma exhumation rates were relatively slow ~0.1 mm/yr.), from ca. 2–1.5 Ma to ca. 0.5 Ma (rates increased to 2–4 mm/yr.), and from ca. 0.5 Ma to present rates accelerated to 4–8 mm/yr. The rate of this most recent, relatively rapid increase in exhumation in the southern Central Range is consistent with geodetic and seismic data that show active uplift of the range. The brittle structures that accommodated this rapid exhumation, however, are still unknown.

3. Regional- and outcrop-scale faults in the southern central range

To understand the origin of the gradient in the rate of uplift along the Southern Cross-Island Highway (SXIH) identified by the leveling surveys (Fig. 1C; Ching et al., 2011; Hsu et al., 2018), we integrated a detailed analysis of fault data collected along the Xinwulu and Dalun Rivers and along a 32 km section of the SXIH (Fig. 1B) with a regional-scale study of the southeast part of the range using a 6 m three digital elevation models (DEMs) (https://landslide.geologycloud.tw/map/zh-tw) and two UAV studies along the ridge crest (Fig. 1A and white colour mountain in Fig. 1B). Although these studies cover significantly different spatial scales they yield a consistent pattern of stress and strain. We also include a discussion of GPS and earthquake focal mechanisms to show consistency with the current stress and strain fields. Taken together, these integrated data sets suggest substantial lateral and vertical movement of the upper and lower crust.

3.1. Outcrop-scale fault data

All of the river and highway field sites are located in low to moderate-grade metamorphic rocks such as metasandstone, slate, and schist (Fig. 2). In total, 164 faults were identified in the field, 141 of which consist of striations and slip-sense indicators (Table S1). Slip sense was inferred using various indicators, including drag folds, Riedel shears, tool marks, quartz slickenfibers, slickenside lineations, and offset marks (Fig. 3). Of the 141 faults, 48 are strike-slip faults, and 93 are normal faults (Table S1). In order to aid in the identification of scattered fault populations associated with a particular stress tensor, we

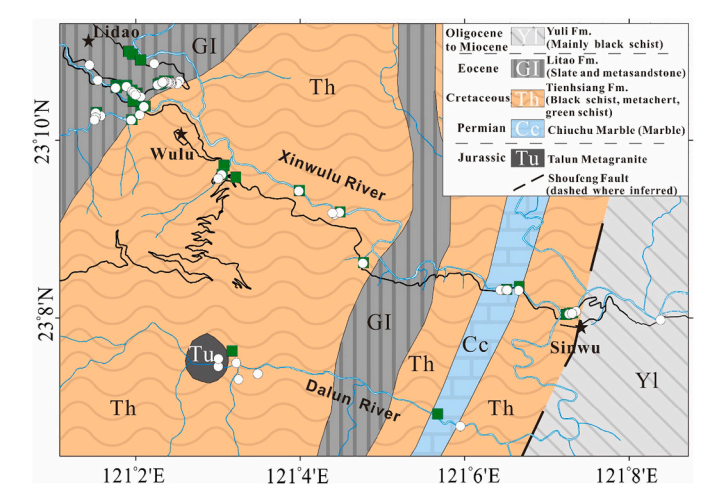


Fig. 2. Geologic map showing locations of outcrop-scale faults (geology from Lin and Chen (2016). Squares: strike-slip faults; circles: normal faults; black line: Southern Cross-Island Highway.

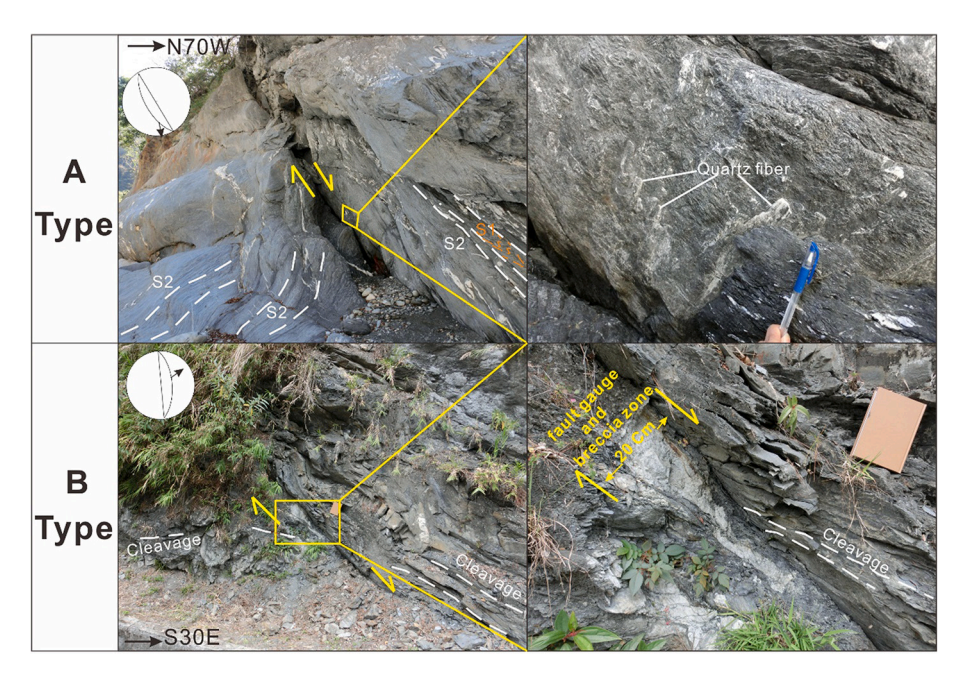


Fig. 3. Field photographs of two typical deformation styles recognized in the field: Faults characterized by calcite or quartz fibers on the fault plane (Type A) and faults characterized by fault gauge or breccia on the fault plane (Type B).

distinguish groups of faults based on crosscutting relationships and the natural material of the fault zone and recognized two styles of deformation: A) faults characterized by stretched calcite or quartz fibers on the fault plane and B) faults characterized by rock-on-rock slickenlines, fault gauge, or/and breccia on the fault plane (Fig. 3). Of the 141 faults, 135 of the faults were classified as B-type whereas 6 of the faults were classified as A-type. Crosscutting relationships indicate that all faults postdate cleavage formation (Fig. 3), however, there is no distinctly consistent crosscutting relationship between two fault types.

3.1.1. Inversion of fault-slip data: methods

The primary aim of paleostress inversion is to determine the orientations of the three principal stresses (maximum σ_1 , intermediate σ_2 , and minimum σ_3) that form the axes of the stress ellipsoid and represent the eigenvectors of the best-fit stress tensor that activated the fault population. In this study, we used the Gauss method to analyze the 141 faults with a known sense of slip, which is based on the direct stress inversion (Angelier, 1994). The advantage of the Gauss method is the ability to isolate homogeneous subsystems within a population of heterogeneous fault data. The Gauss method, based on the direct stress inversion technique (Angelier, 1994), has been implemented in the T-TECTO computer program by Žalohar (Žalohar, 2009). The functions embedded in the Gauss method allow the user to analyze the distribution of angular misfit (α) between the shear stress and actual direction of slip along the faults on the fault plane and separate polyphase fault populations by employing several user-defined parameters (Zalohar and Vrabec, 2007). The essential user-defined parameters of the Gauss method are: Δ , \emptyset 1, \emptyset 2, k, s, where Δ is the threshold value of compatibility, Ø1 is the angle of the internal friction, Ø2 is the angle of friction for sliding on a preexisting fault, k is the stress parameter that weights the importance of friction, and s is a dispersion parameter, which represents the value of the second moment of the distribution of angular misfit between the shear stress and actual direction of slip along the faults. (Žalohar and Vrabec, 2007). In addition, in order to constrain inversion results to mechanically acceptable solutions, the Gauss method considers the ratios between the normal and shear stress on the fault plane consistent with the principles of Mohr-Coulomb failure by plotting the position of the "Mohr point" for each fault on a Mohr diagram. Fault populations outside of a user-defined misfit angle with the first best-fit stress tensor are removed from the data set and analyzed in the same way, to find the second population with the second best-fit stress tensor. The process is repeated until there are no independent populations of faults. The first population with a compatible stress tensor is classified as "phase 1" and the second population is phase 2, and so forth. We limited our analysis to phases with 10 or more faults.

3.1.2. Inversion of fault-slip data: results

Because the field observations of the fault data do not show well-defined cross-cutting relations, we utilize the Gauss stress inversion method to isolate homogeneous subsystems within all fault-slip data. We analyzed all 141 faults with a known sense of slip as depicted in Fig. 4; the results of the Gauss stress inversion method are given in Table 1. Inversion of the 141 faults yielded two phases: Phase 1 contains 84 faults and yields a maximum extension axis that trends sub-horizontally 225° and a maximum shortening direction that plunges 82° to the southeast (Fig. 4). Phase 2 contains 28 faults and with a maximum shortening

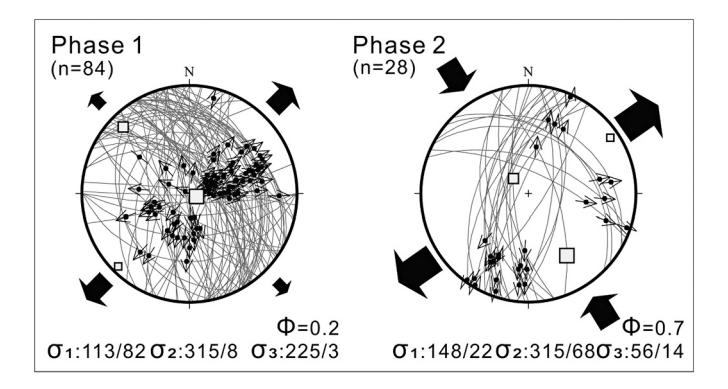


Fig. 4. Paleostress inversion of all the faults suggests two phases of deformation. Phase 1 (i.e., stress state with the most faults) has 84 faults and shows a sub-horizontal extension direction that trends NE as well as sub-vertical shortening. Phase 2 has 28 faults and also shows a sub-horizontal extension direction that trends NE; however, the shortening direction is subhorizontal and trends SE. Both phases show a sub-horizontal extension direction that trends NE which is similar to extension directions determined from GPS (Fig. 8) and earthquake focal mechanisms (Fig. 10).

Table 1Results of Gauss method inversion.

Phase	σ_1	σ_2	σ_3	Φ
1	113°, 82°	315°, 8°	225°, 3°	0.2
2	$148^{\circ}, 22^{\circ}$	315°, 68°	056°, 4°	0.7

Parameters for stress inversion are as follows: $s=15,\,\Delta=30,\,\varnothing 1=60,\,\varnothing 2=20,\,k=20,$ High grid point density.

direction that plunges gently towards 148° and the maximum extension axis that plunges gently to 056° (Fig. 4).

Additional phases contain significantly few faults and show less well-defined patterns shown in Fig. S1: phase 3 contains 10 faults and yields a maximum extension axis that trends sub-horizontally 084° and a maximum shortening direction that plunges 67° to the south; phase 4 contains 9 faults and with a maximum shortening direction that plunges gently towards 294° and the maximum extension axis that trends sub-horizontally 200° ; phase 5 contains 6 faults and with a maximum shortening direction that plunges gently towards 214° and the maximum extension axis that plunges gently towards 116° .

3.2. Regional-scale faults

To complement the detailed field studies, we identified and mapped additional structures that represent potential regional-scale faults using DEMs supplemented with field observations where possible. Two of the DEMs are based on Lidar data collected by the Central Geological Survey (CGS) in Taiwan with a 6 m resolution (Figs. 5 and 7) (https://landslide.geologycloud.tw/map/zh-tw). Two additional DEMs were constructed from photomosaics collected with a UAV during two field expeditions to the area around Jianming Lake (Fig. 6). The DEMs from the Jianming Lake area were constructed using a UAV and Pix4Dmapper which is an application in Pix4D software suite (Computer Vision Lab in

Switzerland; http://pix4d.com). Pix4Dmapper includes rayCloud, which extends the 3D triangulation and increases the accuracy of modeling results (Ruzgienė et al., 2015). 285 and 300 images were converted in the western (Fig. 6A) and eastern (Fig. 6C) areas respectively.

In both the CGS and UAV DEMs data sets potential faults were identified as relatively straight lineaments in the topography that appear to cross-cut and offset stream valleys or intervening ridges. The attitudes of potential faults identified in the DEMs were estimated by importing kmz files into Google Earth and mapping the fault traces across differences in elevation. These differences were then used to construct a 3point problem that defined the strike and dip of the fault (detail data can be found in the Supplementary material, Table S2). Lineaments identified in the DEMs and inferred to be faults are shown in Figs. 5 and 7; about 70% of the identified lineations yielded fault attitudes. In a few areas, subtle changes in grayscale also form lineations in map view and appear to represent planar features. These features, however, do not appear to offset ridges or valleys and appear to have 3-D geometries consistent with structural fabrics observed in the area (see lithologic layering and cleavage data in Table S3). These lineaments are therefore inferred to be metamorphic layering rather than faults.

The area around Jianming Lake shows several north-northeast to north-northwest trending lineaments that appear to be faults (Fig. 5). Structural analysis shows that the structures typically dip from 30° to 50° (Fig. 5; Table S2) and have normal displacements. These attitudes and kinematics are similar to the Phase 1 faults observed in the field (Fig. 4) but inconsistent the orientations of lithologic layering and penetrative fabrics mapped in the area.

In the UVA survey area west of Jiaming Lake (Fig. 6A), two subparallel lineaments trend NNE-NNW and are associated with eastdipping fault plane (Fig. 6A), the outcrop of one of the two fault scarps at the Jiaming Lake trail junction (white star) shows a steep, eastfacing surface slope, the hanging wall lower the footwall suggesting an

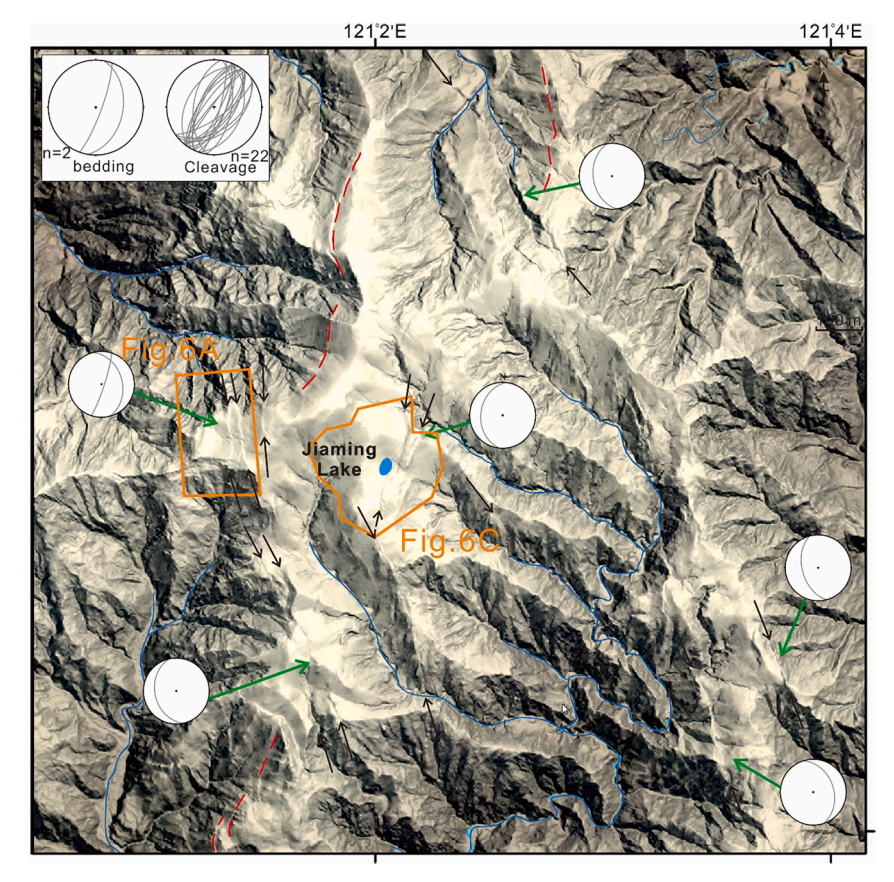


Fig. 5. Topography and lineaments of field area near Jiaming Lake. Black arrows show the locations and trends of the faults; Red dashed lines show trace of bedding. Orange polygons show locations of UAV surveys (see next figure). Stereonets show the strike and dip derived from three different elevation points on individual fault planes (detailed data can be found in the Supplementary material, Table S2). (For interpretation of the references to colour in this figure legend, the reader is referred to the web version of this article.)

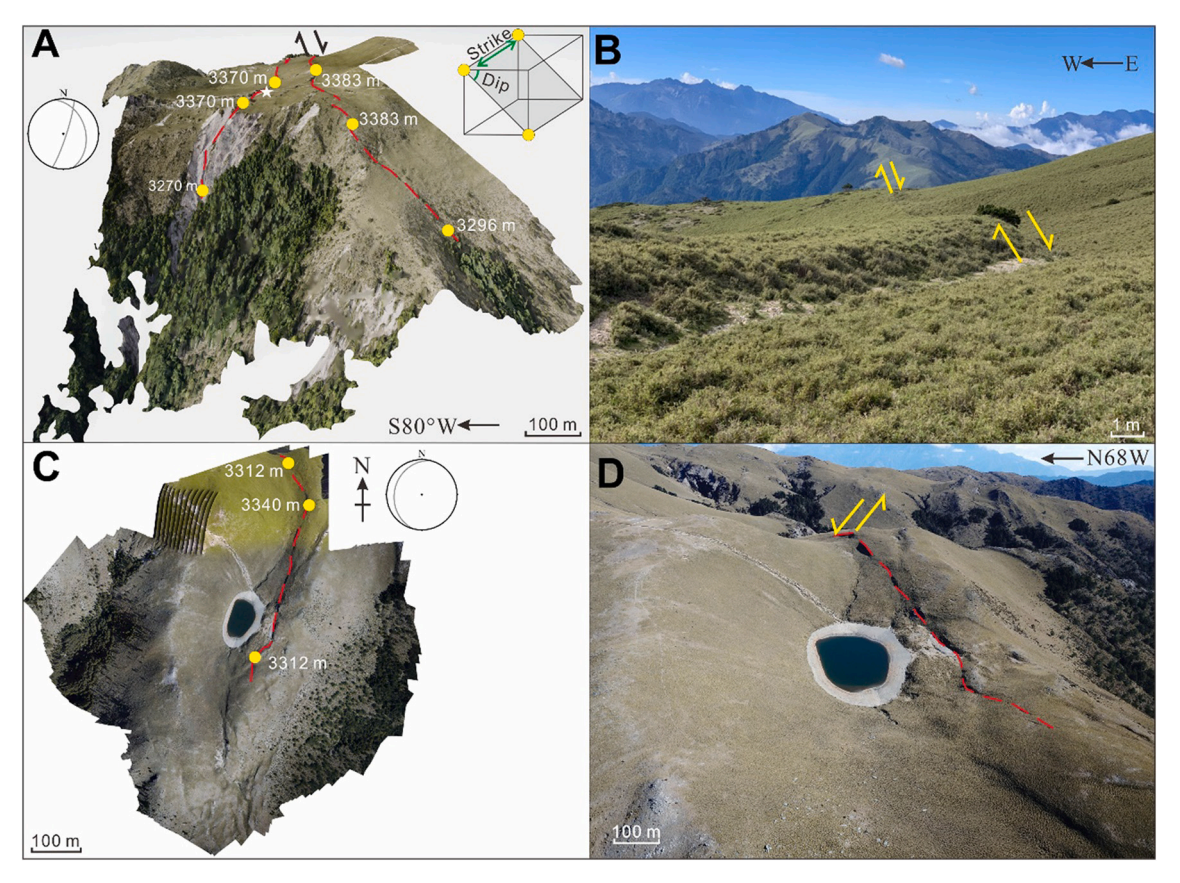


Fig. 6. 3D models of topography based on UAV surveys and field photographs near Jiaming Lake. (A) 3D model of the western area shows two subparallel lineaments (red dash line). Three different elevations along the faults (yellow points) indicate east-dipping fault planes (detail data can be found in Table S2). (B) Outcrop photograph western fault in (A), white star; north view, showing steep, east-facing slope. The footwall 1 m higher than the hanging wall suggesting an east-dipping normal fault. (C) 3D model of the area around Jiaming Lake showing a lineament, trending NNE. Three different elevations along the faults (yellow points) suggests a northwest-dipping fault plane (detail data can be found in Table S2). (D) Outcrop photograph around Jiaming Lake; northeast view, showing west-facing slope. The footwall is higher than the hanging wall suggesting west-dipping normal fault. (For interpretation of the references to colour in this figure legend, the reader is referred to the web version of this article.)

east-dipping normal fault (Fig. 6B). In the area east of the lake (Fig. 6B), the UAV survey revealed a NNE-trending lineation that appears to represent a west-dipping normal fault (Fig. 6C), suggesting that the lake has formed in graben or sag pond between adjacent faults.

An additional suite of lineaments and planar surfaces was identified in the area of the Chingsuei River east of the Jiaming Lake using the Lidar-based DEMs (Figs. 1 and 7). The DEM shows several south-dipping triangular-shaped slopes generally aligned parallel to each other are highlighted in Fig. 7. Additional surfaces with similar geometries appear to offset the interfluves north of the river and further upstream (background in Fig. 7). The remote location, dense vegetation, and rugged terrane limited field observations but data from the large facet in the foreground of Fig. 7A show evidence of a south-dipping normal fault (Table S1). Several additional locations along the river also show evidence for late-stage northeast-southwest extension (Fig. 7). We, therefore, interpret the east-west striking faceted topography as evidence of regional-scale normal fault that offsets the generally north-trending ridges or interfluves. The systematic decrease in elevation from north to south along the ridge crest near the contact between the Tailuko and Yuli Belts (Fig. 7) suggests several hundred meters to a kilometer of offset, which is consistent with the apparent offset of the quartz-mica schist member of Yuli Belt (Lin et al., 1984) in the foreground of Fig. 7. The geometries and kinematics of the proposed faults are also consistent with Phase 1 of the faults measured along the SXIH (Fig. 4).

4. Surface strain-rate derived from GPS

To illustrate the surface strain rate field in southern Taiwan, we computed the 2D strain from the cGPS velocity field (Chen et al. (2017) using SSPX software (Cardozo and Allmendinger, 2009). Strain was computed using the Grid-Nearest Neighbor routine with a 10 km grid spacing, 6 neighbors, and a maximum radius of 30 km. The velocity field (relative to station TENC, near the top of Southern Cross-Island Highway), dilatation rate and extension axes are shown in Fig. 8A. With respect to Central Range, the stations in the fold-and-thrust belt and the Coastal Range show motions towards the Central Range. Stations within the southern Central Range and the southwest fold-and-thrust belt, however, show motions towards the southwest. Negative dilatation (contraction) occurs in western and eastern Taiwan, whereas positive dilatation (extension) occurs in the middle and southern Central Range (Fig. 8B). Positive dilatation is also present in the Ilan Plain and the area of the Okinawa Trough in northern Taiwan. The trends of the extension axes in central and southern Taiwan show three general patterns: N-S to NNE trends in western central Taiwan; E to ENE trends in southern Taiwan and a zone that grades between these two patterns in southwest Taiwan where extension trends NE. The dilatation rate combined with the extension direction suggest southwest movement of at least the upper crust.

5. Stress analysis of earthquake focal mechanisms

In order to know the spatial distribution of stress states in the crust,

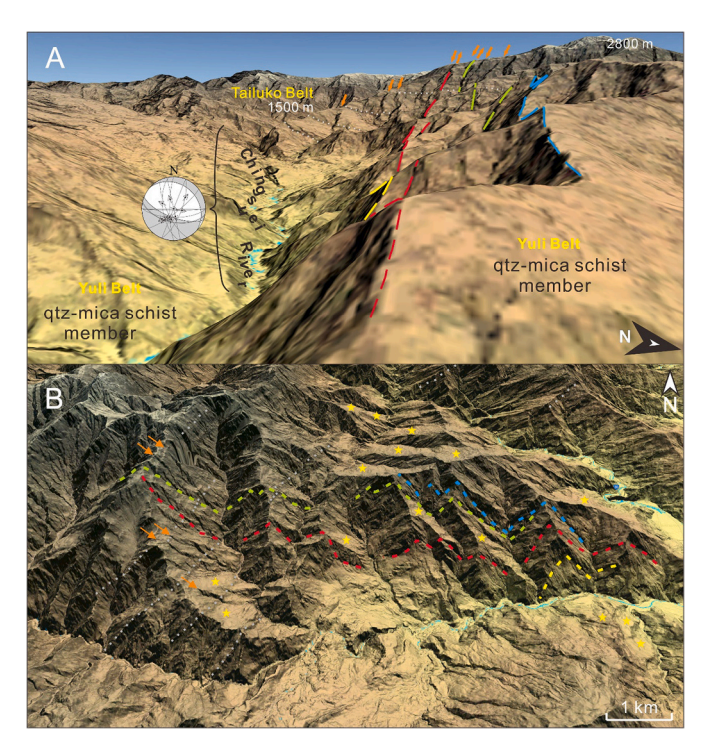


Fig. 7. Two Lidar-based DEMs overlain on Google Earth images of the area around the main truck of the Chingsuei River. Dashed lines highlight aligned faceted slopes with colors showing proposed correlations. Dotted line shows the trace of metamorphic layering. (A) west view; (B) east view. Illumination is from the north in both images. Stereonet in (A) shows strike, dip and offset (arrow shows motion of hanging wall) of late-stage faults along the river; shaded areas represent quadrants of instantaneous compression in a kinematic model of failure for the faults; associated extension direction trends NE-SW. These data, the apparent offsets of the interfluves, and the co-planarity of the faceted topography suggest the Chingsuei River follows a regional-scale south-side down normal fault.

we used first-motion polarities of P waves from Wu et al. (2008) to determine the focal mechanism solutions for earthquakes. We chose events with magnitudes ML \geq 4.0 from the Central Weather Bureau (CWB) catalog. Wu et al. (2008) implemented a genetic algorithm in a nonlinear global search for the focal-mechanism solutions (Wu et al., 2008). The earthquakes we used occurred in the southern Taiwan region between 1991 and 2016. We used the algorithm from Angelier (1979) to resolve the principal stress axes of the focal mechanisms of earthquakes, and delineated four deformation domains based primarily on earthquake kinematics: 1) Northwest (NW domain); 2) Central (CR domain); 3) Southwest (SW domain) and 4) Southeast (SE domain) (Fig. 9). To understand the vertical variations in stress, particularly an anomalous zone of NE-SW shortening in southwest Taiwan, we also analyzed the principal stress axes in four layers from 0 to 40 km depth in the southwest domain.

As shown in Fig. 9, earthquake focal mechanisms show normal, strike-slip, and thrust faults around the southern Central Range; the earthquakes in the NW, SW, and SE domain are dominated by strike-slip and thrust faulting, whereas the CR domain is dominated by strike-slip and normal faulting. This variation corresponds to thrust faulting and strike-slip faulting in the crust below lower elevations (below 1000 m) and normal faulting and strike-slip faulting in the crust below higher elevations (Fig. 9). The earthquakes are generally distributed between 1 and 30 km in depth except in the central domain where they are generally $<\!10\,\mathrm{km}$. We suggest it is noteworthy that the earthquakes with normal and strike-slip faulting mechanisms beneath the southern Central Range are restricted to shallow depths.

Here, we perform stress analysis for different dominant types of focal

mechanisms in the four domains (Fig. 10). In the northwest domain, the strike-slip faults show a NW-SE shortening (mean trend of 293°) and NE-SW extension (mean trend of 047°), and the thrust faults that show a NW-SE shortening (mean trend of 297°). In the southeast domain, the strike-slip faults show a NW-SE shortening (mean trend of 147°) and NE-SW extension (mean trend of 053°), and the thrust faults, show a NW-SE shortening (mean trend of 122°). Both domains show significant NW-SE compression subparallel to Philippine Sea plate motion relative to Eurasia. In the central domain, the strike-slip faults show a NW-SE shortening (mean trend of 125°) and NE-SW extension (mean trend of 220°), and the normal faults, show a NE-SW extension (mean trend of 047°). In the southwest domain, the strike-slip faults show NE-SW shortening (mean trend of 243°) and NW-SE extension (mean trend of 142°), and the thrust faults, show ENE-WSW shortening (mean trend of 265°). Overall, we document northwest-directed shortening in all areas except in the southwest domain where shortening is northeast-directed. The northeast-directed extension in the upper crust of the central domain, is consistent with our field data. The northwest shortening of the northwest and southeast domains is deeper and reflects deformation of the

In order to examine the vertical distribution of stress and fault types in the southwest domain, we separated the focal mechanism into four depth layers above the 40 km (Fig. 11). Earthquakes between 0 and 20 km accommodate predominantly a mixture of reverse and strike-slip faulting, with only three events accommodating normal faulting between 10 and 20 km and only two accommodating reverse faulting between 0 and 10 km. The 20-30 km depth range is similarly dominated by a mixture of reverse and strike-slip faulting. Between 30 and 40 km, however, only 4 earthquakes reflect strike-slip faulting. Our finding of strike-slip faulting is similar to the result for different magnitudes of earthquakes in the southwest domain by Chen et al. (2017). In Fig. 11, the trend of the shortening direction differs slightly between strike-slip and thrust fault. For strike-slip faulting our results indicate NE shortening between depths of 10-30 km and NNE shortening between depths of 30-40 km, whereas for thrust faulting we find NW shortening shallower than 10 km and ENE shortening between depth of 10-40 km. Overall, the shortening varies from NW to NE to NNE, from the surface to 40 km depth.

6. Discussion

6.1. Relative age of late-stage structures

Kinematic analysis of the field-based fault data indicates two phases of deformation, with phase 1 dominated by normal fault kinematics and phase 2 dominated by strike-slip kinematics (Fig. 4). Although we were not able to identify distinct crosscutting relations between the two phases, cross-cutting relations were observed or reasonably inferred along the western (Huang and Byrne, 2014) and central sections of the Southern Cross-Island Highway (Fig. 1B) (Crespi et al., 1996), and in the southern Central Range south of the study area (Mesalles, 2014). Applying these relations to the study area is consistent with the abundant evidence of normal slip in the area of Jiaming Lake (Fig. 5), the offset ridges and truncated spurs along the north bank of the Chingsuei River (Fig. 7) and the kinematics obtained from earthquake focal mechanisms in the upper crust of the southern Central Range (CR domain in Figs. 9 and 10). Taken together, the observations from the southern Central Range suggest that the upper crust is experiencing northeast-southwest extension and that this deformation was proceeded by conjugate strike-slip deformation that also was associated with northeast-southwest extension.

6.2. Regional-scale interpretations

Previous studies suggest that the extension in the Central Range resulted from: 1) tectonic extension driven by buoyancy forces or stress

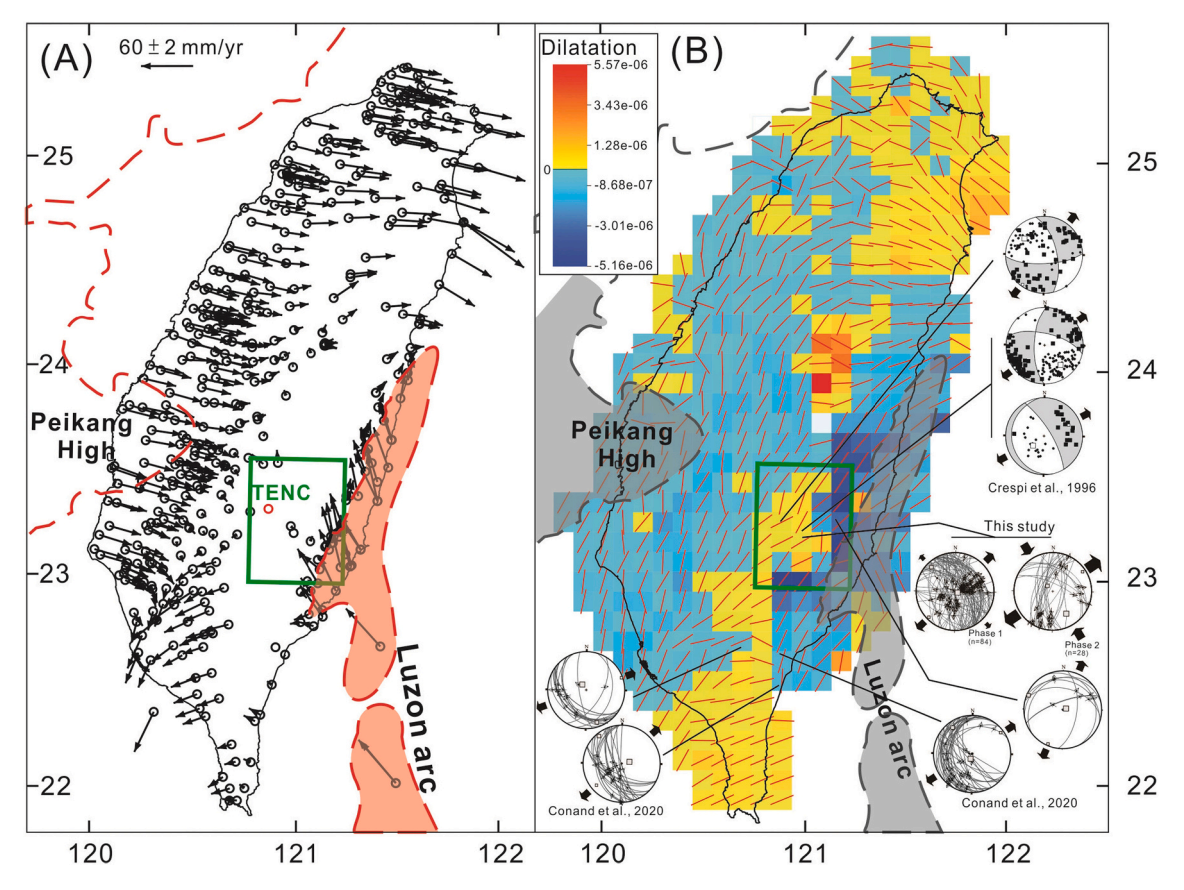


Fig. 8. The cGPS velocity field from Chen et al. (2017) included 425 cGPS sites from 1994 to 2015 that were collected by the Institute of Earth Sciences, Academia Sinica. (A) The GPS velocity field relative to station TENC, near the ridge crest along Southern Cross-Island Highway. (B) Dilatation and principal strain rate. The colour scale indicates dilatation rate (positive = dilatation, negative = contraction). Red line segments denote the trend of the maximum extension strain-rate axes. Green box shows the field study area. Stereonets show the field faults data from this study, Crespi et al., 1996 and Conand et al., 2020. (For interpretation of the references to colour in this figure legend, the reader is referred to the web version of this article.)

gradients (e.g., Chen et al., 2018; Lin, 2000), 2) gravitational collapse as the crust is over thickened by underplating (Crespi et al., 1996; Hsu et al., 2009), 3) regional-scale folding above a bending detachment (e.g., Carena et al., 2002), or 4) transtensional brittle deformation (Conand et al., 2020). Considering that the first three mechanisms predict extension orthogonal to the orogen (i.e., WNW to ESE), which is inconsistent with the results presented here, we first evaluate the transtensional model, then evaluate two alternative interpretations: gravitational collapse towards the SCS and tectonic extrusion orthogonal to the plate convergence vector.

Conand et al. (2020) proposed that extension in the Backbone Range was associated with regional-scale strike-slip deformation resulting from oblique convergence. The relatively small angle between the plate convergence vector and the orogen ($\sim\!15^\circ$ to 20°), however, would favor oblique subduction rather than any form of strain partitioning in the hanging wall (see for e.g., McCaffrey, 1992). GPS data in the core of the orogen also indicate shortening rather than transtension (Fig. 8B), suggesting that if transfension is a dominant process, it is limited to the southern Backbone Range. In addition, to our knowledge active regional-scale, strike-slip faults with significant offset have not been recognized in the orogen, although some faults have a component of oblique slip (e.g., the Longitudinal Valley fault). Finally, in the transtension model, normal faults and strike-slip faults with oblique-normal slip would appear to form contemporaneously and this is inconsistent with available observations that show cross-cutting relations (Crespi et al., 199; Huang and Byrne, 2014; Mesalles, 2014).

An alternative interpretation, is that Conand et al.'s data record two events: early, NW-SE shortening accommodated by conjugate strike-slip fault deformation followed by NE-SW extension accommodated by

normal faulting.

6.3. Gravitational flow to the southwest

We evaluate the gravitational flow of the orogen by comparing differences in gravitational potential energy (GPE) in the southern Central Range to the GPE of the South China Sea. The overall concept is that when comparing the GPE between any two columns of continental lithosphere, the column with the greater gravitational potential energy exerts a horizontal compressive deviatoric stress on the column with the lower gravitational potential energy (Platt and England, 1994). Thickening of the crust and growth of orogenic topography during the collision would have increased the gravitational potential energy in the Central Range (Lo and Hsu, 2005), and this difference in gravitational potential energy may cause material to flow in the SW direction, towards the South China Sea with a lower gravitational potential energy. It can be expressed by estimating the difference in gravitational potential energy between columns of the lithosphere in the southern Central Range and the South China Sea lithosphere. The method of calculation in this paper follows Molnar and Lyon-Caen (1988):

$$\Delta \text{GPE} = \int_{-h}^{H_0 + \Delta H} \rho_c g(x) dx - \left[\rho_{\scriptscriptstyle W} g(x) + \rho_c g(x) + \rho_{\scriptscriptstyle m} g(x) \right] dx$$

where ρ_c is the density of the crust, ρ_w is the density of the water, ρ_m is the density of the mantle, g is the gravitational acceleration, h is the elevation, H_0 is the crustal thickness, and ΔH is the thickness of the crustal root. Given h=2.5 km, H_0 =30 km, ΔH =10 km, ρ_c =2750 kg m^{-3} , ρ_m =3400 kg m^{-3} , ρ_w =1050 kg m^{-3} , and water depth is 3 km (Hsieh and

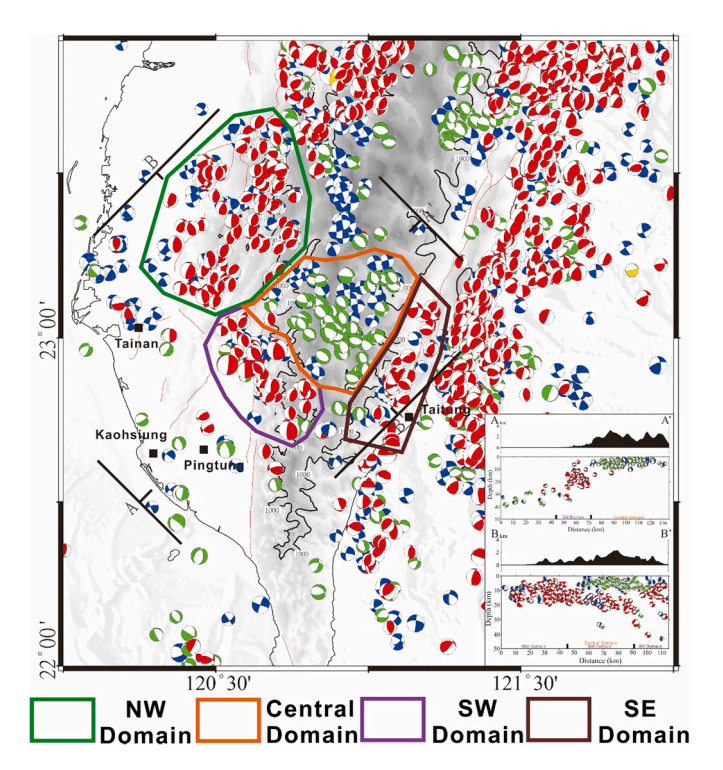


Fig. 9. Earthquake focal mechanisms (ML > 4). Earthquake focal mechanisms show normal (green), strike slip (blue), and thrust (red) faults around the southern Central Range; thrust faults dominate lower elevations (below 1000 m) whereas normal and strike-slip mechanisms dominate higher elevations. Four deformation domains based primarily on earthquake kinematics are shown: northwest domain (green); central domain (orange); southwest domain (purple) and southeast domain (brown). Kinematic data are shown in Fig. 10; A-A' and B-B' profiles are shown in Fig. 12. (For interpretation of the references to colour in this figure legend, the reader is referred to the web version of this article.)

Yen, 2016; Kuo-Chen et al., 2012; Zhao et al., 2010).

We estimate the difference in gravitational potential energy between the southern Central Range and the South China Sea is about $1.64x10^{12} \text{Nm}^{-1}$ (Fig. 12) which is consistent with the ΔGPE reported in Chiang et al. (2016). This value is lower than the ΔGPE between Tibet and Asia lithosphere (7.2x10^{12} \text{Nm}^{-1}), as well as lower than the ΔGPE

between the pre-extended back-arc basins and its surrounding lithosphere (5.5–7.0x10 $^{12} \rm Nm^{-1}$) in the world (Platt, 2007). In addition, it is also lower than the ΔGPE in the present-day extended back-arc basins, such as Basin and Range Province (2.2x10 $^{12} \rm Nm^{-1}$), and the Mediterranean region (2.5x10 $^{12} \rm Nm^{-1}$) (Platt, 2007). However, the possibility of southwest extrusion of the southern Central Range, and by association NE extension in the upper crust is by gravitational collapse to the southwest, cannot be ruled out but the lower value suggests that its importance is relatively low.

6.4. Tectonic extrusion

As an alternative interpretation based on the stress patterns interpreted from field and earthquake data (Figs. 4, 9 and 10), and building on the analysis of non-volcanic tremors in the core of the range (Chen et al., 2018; Ide et al., 2015), we propose that NE-SW extension in the upper crust is driven by the tectonic extrusion of lower crust towards the SW. We propose that as the north-trending Luzon Arc collides obliquely with the ENE-trending Peikang High, the southern Central Range is compressed between the NW and SE domains (Fig. 13A). Following Chen et al., 2018 and Ide et al., 2015, we propose that the tremors are part of a crustal-scale detachment that is imbricating the lower and middle crust. In this interpretation, pro-grade metamorphism may have released fluids that migrate vertically through a system of normal faults in the upper crust. We propose, here, that the detached block of crust recognized by Chen et al., 2018 may also be moving southwest perpendicular to the plate convergence direction and parallel to the subtle change in GPE. We base this interpretation primarily on the evidence for NE-SW extension in the upper crust. Vertical and lateral movement of the crust, however, is also consistent with evidence for relatively high heat flow, low Q (Lee et al., 2010; Wang et al., 2010), low resistivity (Bertrand et al., 2012; Chiang et al., 2010), and a high geothermal gradient (Hsieh et al., 2014) at the northeastern end of the proposed extruding crust.

6.5. Comparison with numerical modeling

Finally, it is also insightful to compare the tectonic extrusion interpretation with numerical models of continental collisions. For example, Seyferth and Henk (2004) constructed a 3-D thermomechanical model using the finite element method and evaluated a range of parameters and boundary conditions. Their basic or "standard" model (S-1) included orthogonal convergence and a free lateral margin. The free

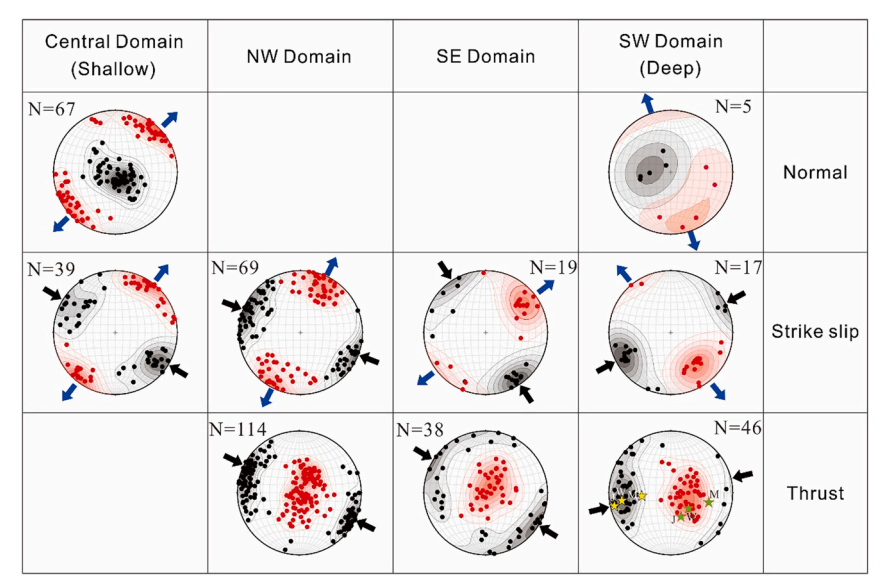


Fig. 10. Stress analysis of earthquake focal mechanisms (4 domains, in Fig. 9) showing: NE extension in the upper crust of the central domain, consistent field data; NW shortening in lower crust of the northwest domain and southeast domain, whereas an anomalous NE shortening in the lower crust of the southwest domain. Red and black dots represent the T-axis and P-axis, respectively. Stars represent the Meinong, Jiaxian, and Wutai earthquake. (For interpretation of the references to colour in this figure legend, the reader is referred to the web version of this article.)

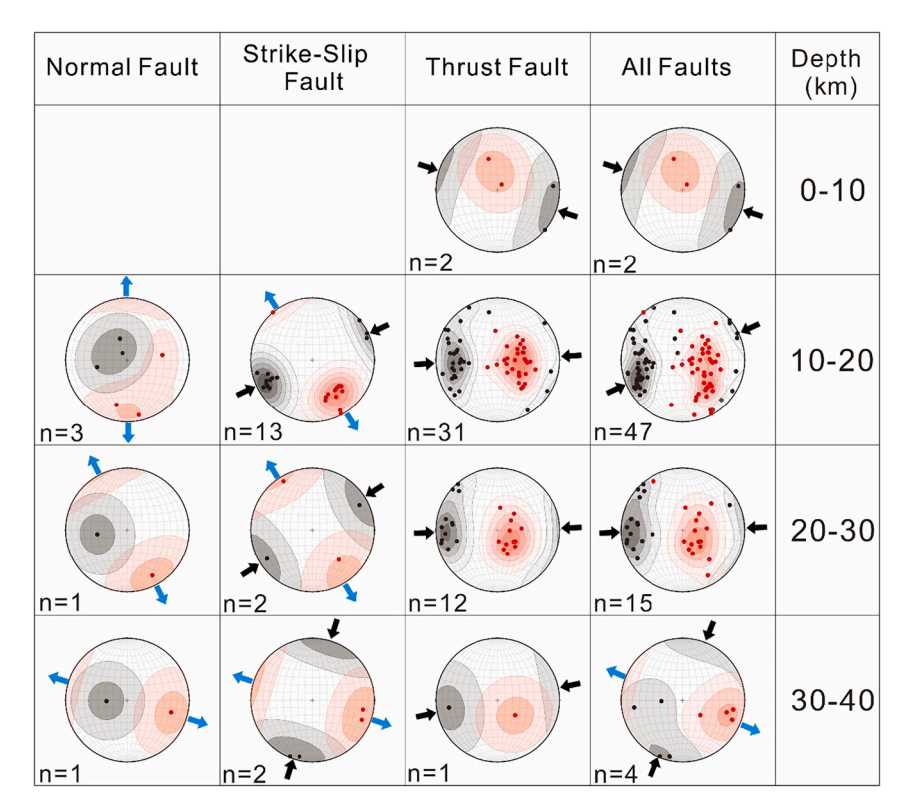


Fig. 11. Stress analysis of earthquake focal mechanisms in four depth layers in the SW domain and each depth interval is 10 km. Red and black dots represent the T-axis and P-axis, respectively. The shortening goes from NW to NE to NNE, from the surface to 40 km depth. (For interpretation of the references to colour in this figure legend, the reader is referred to the web version of this article.)

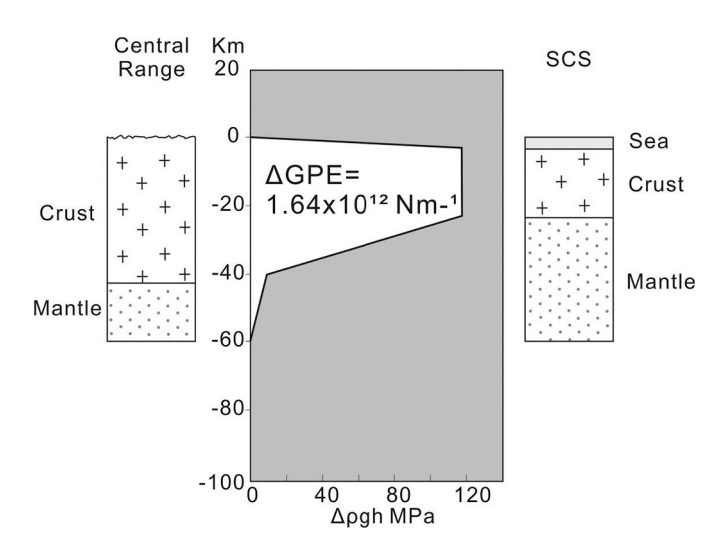


Fig. 12. Plots of gravitational potential energy difference (Δ GPE) between the Central Range and the South China Sea. The difference in lithostatic pressure in MPa (horizontal axis) with depth in km (vertical axis). The integral of $\Delta\rho$ gh with depth (white area) is the Δ GPE (units of 10^{12} Nm $^{-1}$).

lateral boundary condition is particularly relevant to southern Taiwan as it may simulate the transition from the subduction of continental lithosphere in the southern Central Range to the subduction of oceanic lithosphere in the South China Sea south of the collision. Other models included variations in crustal temperature, rheology, convergence rate, and crust-mantle coupling. All of the models were run for 10 Ma and 200 km of convergence and yielded data sets on the spatial and temporal evolution of stress, strain, displacement and temperature. Although their results show substantial spatial and temporal variations in stress

and strain, nearly all of the models show orogen-parallel extension, even during early stages of convergence, consistent with observations in Taiwan.

In comparing the different models in Seyferth and Henk (2004) to the observations in southern Taiwan in more detail, southern Taiwan generally lacks the high topography predicted in most of the models and southern Taiwan records significant orogen-parallel shortening in the transitional zone between collision and subduction (Figs. 10, 11 and 13; Chen et al., 2017). The relatively subdued topography in southern Taiwan, however, is consistent with model R-2 where crustal heat flow is relatively high compared to the classic model (S-1). The southern Central Range is also characterized by relatively high heat flow (Bertrand et al., 2012; Chen et al., 2018; Chiang et al., 2010; Hsieh et al., 2014; Lee et al., 2010; Wang et al., 2010), suggesting that lateral flow of thermally weakened crust may account for the subdued topography in southwest Taiwan.

6.6. Implications and prediction tectonic extrusion

An additional aspect of the numerical modeling results is the predicted development of strike-slip faults on the east and west sides of the extruding block in southern Taiwan. Lacombe et al. (2001) also recognized the importance of strike-slip faults in accommodating crustal extrusion and suggested that their absence in southern Taiwan might be explained by the very recent development of the extruding block. We agree with this interpretation and note that the NE–SW trending Chishan fault, a reverse fault with a right-lateral component (Lacombe et al., 2001), and the left-lateral shear of several watersheds along the eastern flank of the southern Backbone Range (Ramsey et al., 2007) may record the accommodation of the extruding block.

Tectonic extrusion also fails to replicate the orogen-parallel shortening beneath the coastal plain south of the Central Range (see, for example, the Meinong, Jianxing, and Wutai earthquakes in section A-A' Fig. 13) where orogen topography is more subdued. One possible

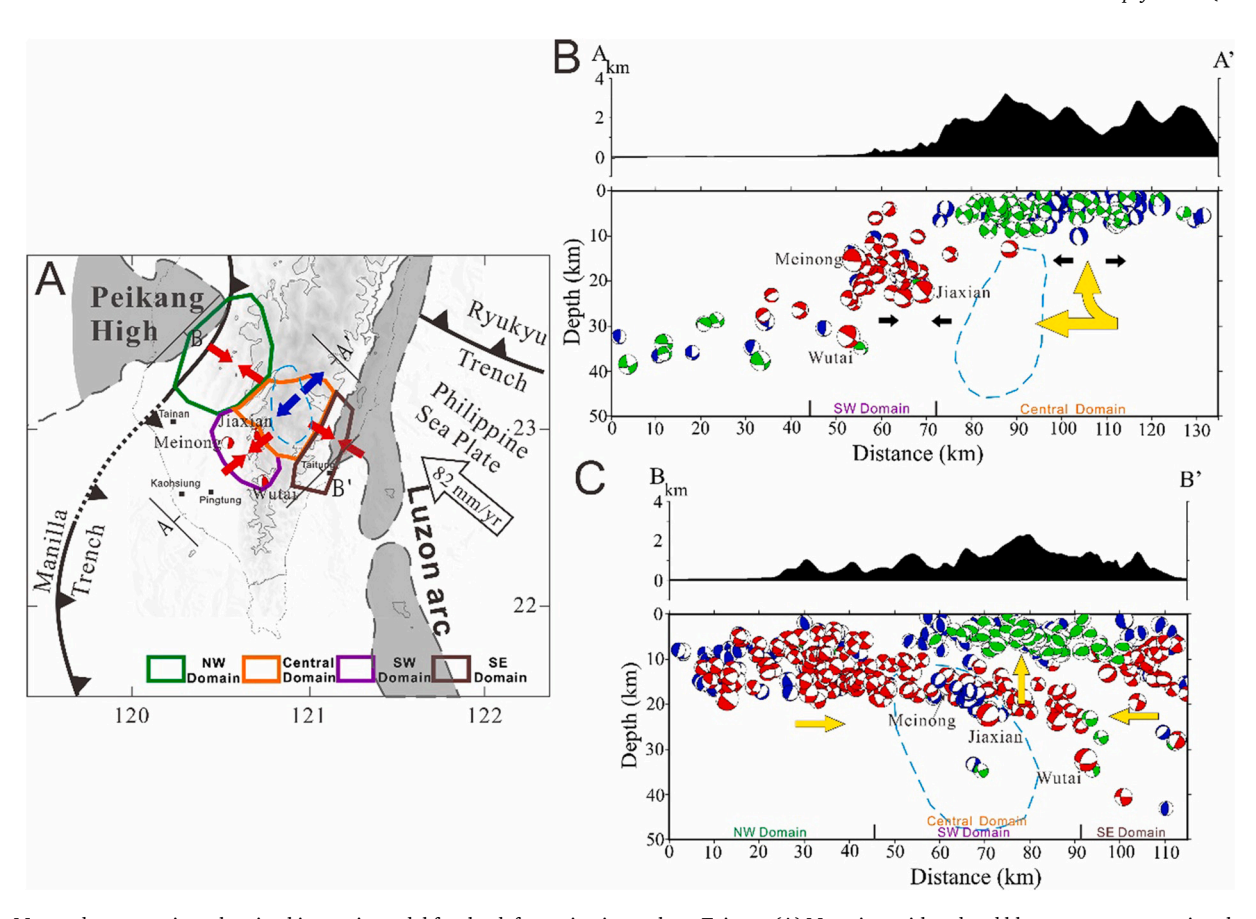


Fig. 13. Map and cross-sections showing kinematic model for the deformation in southern Taiwan. (A) Map view with red and blue arrows representing shorting and extension directions, respectively. Focal mechanisms represent Meinong, Jiaxian, and Wutai earthquakes. (B) Topographic profile and earthquake focal mechanisms along a 40-km wide swath parallel to A-A'. (C) Topographic profile and earthquake focal mechanisms along a 60-km wide swath parallel to B-B'. Red, green, and blue focal mechanisms represent thrust, normal, and strike-slip mechanisms, respectively; Blue dash line represents zone of tremor (Chen et al., 2018); Yellow arrows represent the movement direction of the lower crust beneath the Central Range. (For interpretation of the references to colour in this figure legend, the reader is referred to the web version of this article.)

interpretation is that this zone of mid-crustal shortening may reflect a change in rheology of the lower crust possibly related to lower heat flow away from the orogen, resulting in NE-SW compression in the lower crust.

Southwest extrusion of the lower crust beneath the southwest Taiwan (SW domain) is also inconsistent with the orientation of shearwave (Vs) anisotropy in the crust of Taiwan (Huang et al., 2015). The Vs anisotropy models show the fast directions in the lower crust (13–30 km depth) are parallel to the current plate convergence vector whereas the tectonic extrusion model predicts flow to the southwest. Although a full analysis is beyond this paper, we note that southwest extrusion may have developed relatively recently whereas velocity anisotropies, because they represent penetrative rock fabrics, develop over geologic time (e.g., millions of years).

6.7. Timing of extrusion

All of the normal fault systems described here appear to be relatively young which is consistent with the interpreted onset of extrusion in southwest Taiwan in the late Pleistocene based on offset sediments (Lacombe et al., 2001). Extending the region of extrusion into the southern Central Range, as we are proposing here, allows the application of additional temporal constraints for both extrusion and uplift of the range. For example, Hsu et al. (2016) proposed an acceleration of exhumation cooling at about 0.5 Ma based on totally reset detrital zircon (youngest age: 0.425 Ma) and apatite ages (youngest age: 0.25 Ma) from the area of Small Ghost Lake (location in Fig. 1). A relatively young age

for uplift (and southwest extrusion) is consistent with the southward tilt of watersheds in the southern Central Range (Ramsey et al., 2007) and the progressive increase in rates of erosion and exhumation cooling from the Hengchun Peninsula to the South Cross-Island Highway (Chen et al., 2021; Derrieux et al., 2014).

Another approach to constraining the age of uplift of the southern Central Range is to use the rates of rock uplift along the SXIH, based on leveling data (Hsu et al., 2018). Using a rate of 5–10 mm/yr and the current elevation of the range (\sim 3000 m) suggests uplift may have started 0.7 to 0.3 Ma which is consistent with the zircon and apatite data (Hsu et al., 2016). An intriguing interpretation, therefore, is that the topographic growth of the Central Range occurred less than a million years ago. If this is correct, the growth of the range is substantially younger than the often stated 5–6 Ma initial from north or simultaneous (Lee et al., 2015; Suppe, 1984; Teng, 1990). In this context uplift and southwest extrusion of the southern Central Range may represent southward propagation of the colliding orogen (Suppe, 1981) or a very recent change in the motion of the Philippine Sea Plate relative to Eurasia (e.g., < 1 Ma, Byrne et al., 2019; Wu et al., 2016).

7. Conclusion

The detailed analysis of regional- and outcrop-scale fault data reveals the late-stage brittle faults are predominantly normal faults and have geometries and kinematics that are consistent with leveling, GPS-based strain rate, and earthquake data across the range. The geometry and kinematics are also consistent with stress patterns inferred from ambient

tremors that suggest extension in the upper crust and contraction in the lower crust. Kinematic analysis of field-fault data indicates that the upper crust of the internal area of the southern Taiwan orogen is controlled by a NE-SW extensional stress regime. This NE-SW extension is consistent with the SW direction movement of the lower crust beneath the southern Central Range and contraction direction beneath southwest Taiwan

Based upon analysis of geological, structural, seismic, and geodetic data from southern Taiwan, we propose a tectonic model in which the crust in southern Taiwan is shortened between the obliquely colliding Peikang High and the Luzon Arc and that shortening is accommodated by SW-directed lateral and vertical movement of the lower crust. The normal faults with the northeast extension in the southern Central Range reflect the consequence of the SW lateral and vertical movement of the lower crust. Essentially, the vertical movement of the rocks results in the permutation of the principal stresses through time with σ 1, inferred to be horizontal as the conjugate strike-slip faults formed during NE-SW compression, becoming vertical as the normal faults form. One interpretation of this permutation that is consistent with the states of stress outlined above, is the movement of rocks from the middle to the upper crust as the southern Central Range thickened during convergence. Based on an acceleration of exhumation cooling at about 0.5 Ma in the southern Central Range and the onset of extrusion in southwest Taiwan in the late Pleistocene, we infer that this SW extrusion process may be younger the 0.5 Ma. Finally, this very recent initiation of SW extrusion of lower crust has not significantly shaped the existing structural pattern in the upper crust of southwestern Taiwan. In fact, better understanding the relation between extrusion and the development of the fold-andthrust belt in the western foothills is an area of exciting future research.

CRediT authorship contribution statement

Wei-Hao Hsu: Conceptualization, Formal analysis, Investigation, Writing – original draft, Visualization, Project administration, Supervision. Timothy B. Byrne: Conceptualization, Investigation, Writing – review & editing, Funding acquisition, Project administration, Supervision. Jonathan C. Lewis: Investigation, Writing – review & editing, Funding acquisition, Project administration. Yue-Gau Chen: Resources, Writing – review & editing, Funding acquisition. Po-Yi Yeh: Formal analysis.

Declaration of Competing Interest

The authors declare that they have no known competing financial interests or personal relationships that could have appeared to influence the work reported in this paper.

Data availability

No data was used for the research described in the article.

Acknowledgement

We appreciate the Taiwan Ministry of Science and Technology (grants MOST 107-2116-M-002-015-MY3, MOST 110-2116-M-001-011-MY3, and MOST 109-2811-M-259-513). Research was supported by the US National Science Foundation (EAR-1220453, EAR-1650157 and EAR-1220317). We greatly appreciate the quiet space at NDHU provided by Dr. Chin-Ho Tsai and Dean Wen-Yen Chang during the final stages of manuscript preparation. We also thank Rick Allmendinger generously provided the Stereonet and SSPX programs; Chiu-Lien Chang, Yu-Wei Liu, Chin-Yuan Chen, Allison Berry, Charles Cavallotti, Lindsey Cromwell, and Lauren Donati for their help with data collection in the field; Dr. Yu Wang, Dr. Yu-Ting Kuo, Dr. Wen-Jeng Owen Huang, Dr. Wei-An Chao, Dr. Jui-Ming Chang, and Yu-Cheng Hsu for constructed 3D models of the topography by UAV system.

Appendix A. Supplementary data

Supplementary data to this article can be found online at https://doi.org/10.1016/j.tecto.2022.229562.

References

- Angelier, J., 1979. Determination of the mean principal directions of stresses for a given fault population. Tectonophysics 56, T17–T26.
- Angelier, J., 1994. Fault slip analysis and palaeostress reconstruction. In: Hancock, P.L. (Ed.), Continental Deformation. Pergamon Press, Oxford.
- Angelier, J., Barrier, E., Chu, H.T., 1986. Plate collision and paleostress trajectories in a fold and thrust belt: the foothills of Taiwan. Tectonophysics 125, 161–178.
- Angelier, J., Chang, T.Y., Hu, J.C., Chang, C.P., Siame, L., Lee, J.C., Deffontaines, B., Chu, H.T., Lu, C.Y., 2009. Does extrusion occur at both tips of the Taiwan collision belt? Insights from active deformation studies in the Ilan Plain and Pingtung Plain regions. Tectonophysics 466, 356–376.
- Armijo, R., Tapponier, P., Mercier, J.L., Han, T.L., 1986. Quaternary extension in southern Tibet: field observations and tectonic implications. J. Geophys. Res. 91 (13), 803–813, 872.
- Bennett, R.A., Wernicke, B., Niemi, N., Friedrich, A., Davis, J., 2003. Contemporary strain rates in the northern Basin and range province from GPS data. Tectonics 22.
- Bertrand, E.A., Unsworth, M.J., Chiang, C.W., Chen, C.S., Chen, C.C., Wu, F.T., Türkoğlu, E., Hsu, H.L., Hill, G.J., 2012. Magnetotelluric imaging beneath the Taiwan orogen: an arc-continent collision. J. Geophys. Res. Solid Earth 117.
- Beyssac, O., Simoes, M., Avouac, J.-P., Farley, K., Chen, Y.-G., Chan, Y.-C., Goffe, B., 2007. Late Cenozoic metamorphic evolution and exhumation of Taiwan. Tectonics 26. TC6001.
- Bos, A.G., Spakman, W., Nyst, M.C.J., 2003. Surface deformation and tectonic setting of Taiwan inferred from a GPS velocity field. J. Geophys. Res. Solid Earth 108.
- Byrne, T.B., Wu, J., Kimura, G., 2019. Geologic constraints on motion of the Philippine sea plate during the late Cenozoic: implications of a CCW rotation in the Pleistocene. In: AGU Fall Meeting Abstracts, pp. T21C–0326.
- Cardozo, N., Allmendinger, R.W., 2009. SSPX: a program to compute strain from displacement/velocity data. Comput. Geosci. 35, 1343–1357.
- Carena, S., Suppe, J., Kao, H., 2002. Active detachment of Taiwan illuminated by small earthquakes and its control of first-order topography. Geology 30, 935–938.
- Chai, B.H.T., 1972. Structural and tectonic evolution of Taiwan. Am. J. Sci. 272, 389–422.
- Chang, C.P., Chang, T.-Y., Angelier, J., Honn, K., Lee, J.-C., Yu, S.-B., 2003. Strain and stress field in Taiwan oblique convergent system: constraints from GPS observation and tectonic data. Earth Planet. Sci. Lett. 214, 115–127.
- Chen, C.-H., 1994. Metamorphic facies map of Taiwan. In: Special Publication of the Central Geological Survey, 2, pp. 1–3.
- Chen, C.-H., 2000. Geologic map of Taiwan. In: Central Geological Survey. Ministry of Economic Affairs.
- Chen, S.K., Wu, Y.-M., Hsu, Y.-J., Chan, Y.-C., 2017. Current crustal deformation of the Taiwan orogen reassessed by cGPS strain-rate estimation and focal mechanism stress inversion. Geophys. J. Int. 210, 228–239.
- Chen, K.H., Tai, H.-J., Ide, S., Byrne, T.B., Johnson, C.W., 2018. Tidal modulation and tectonic implications of tremors in Taiwan. J. Geophys. Res. Solid Earth 123, 5945–5964.
- Chen, A.T., Shen, C.C., Byrne, T.B., Sano, Y., Takahata, N., Yang, T.F., Wang, Y., 2019. Mantle fluids associated with crustal-scale faulting in a continental subduction setting, Taiwan. Sci. Rep. 9, 10805.
- Chen, C.-Y., Willett, S.D., Christl, M., Shyu, J.B.H., 2021. Drainage basin dynamics during the transition from early to mature orogeny in Southern Taiwan. Earth Planet. Sci. Lett. 562, 116874.
- Chevalier, M.L., Tapponnier, P., van der Woerd, J., Leloup, P., Wang, S., Pan, J., Bai, M., Kali, E., Liu, X., Li, H., 2020. Late quaternary extension rates across the northern half of the Yadong-Gulu Rift: implication for east-west extension in southern Tibet. J. Geophys. Res. Solid Earth 125 e2019JB019106.
- Chiang, C.-W., Chen, C.-C., Unsworth, M., Bertrand, E., Chow-Son, C., Kieu, T.D., Hsu, H.-L., 2010. The deep electrical structure of southern Taiwan and its tectonic implications. TAO. Terr. Atmos. Ocean. Sci. 21, 8.
- Chiang, P.-H., Hsu, Y.-J., Chang, W.-L., 2016. Fault modeling of the 2012 Wutai, Taiwan earthquake and its tectonic implications. Tectonophysics 666, 66–75.
- Ching, K.-E., Hsieh, M.-L., Johnson, K., Chen, K.-H., Rau, R.-J., Yang, M., 2011. Modern vertical deformation rates and mountain building in Taiwan from precise leveling and continuous GPS observations, 2000–2008. J. Geophys. Res. 116.
- Chuang, L.Y., Chen, K.H., Wech, A., Byrne, T., Peng, W., 2014. Ambient tremors in a collisional orogenic belt. Geophys. Res. Lett. 41, 1485–1491. https://doi.org/ 10.1002/2014GL059476.
- Clark, M.B., Fisher, D.M., Lu, C.-Y., 1992. Strain variations in the Eocene and older rocks exposed along the central and southern cross-island highways, Taiwan. Acta Geol. Taiwan. 30, 1–10.
- Conand, C., Mouthereau, F., Ganne, J., Lin, A.T., Lahfid, A., Daudet, M., Mesalles, L., Giletycz, S., Bonzani, M., 2020. Strain partitioning and exhumation in oblique Taiwan collision: role of rift architecture and plate kinematics. Tectonics 38. https:// doi.org/10.1029/2019tc005798.
- Coney, P.J., Harms, T.A., 1984. Cordilleran metamorphic core complexes: Cenozoic extensional relics of Mesozoic compression. Geology 12, 550–554.
- Crespi, J., Chan, Y.-C., Swaim, M., 1996. Synorogenic extension and exhumation of the Taiwan hinterland. Geology 24, 247–250.

- Dalmayrac, B., Molnar, P., 1981. Parallel thrust and normal faulting in Peru and constraints on the state of stress. Earth Planet. Sci. Lett. 55, 473–481.
- Derrieux, F., Siame, L.L., Bourlès, D.L., Chen, R.-F., Braucher, R., Léanni, L., Lee, J.-C., Chu, H.-T., Byrne, T.B., 2014. How fast is the denudation of the Taiwan mountain belt? Perspectives from in situ cosmogenic 10Be. J. Asian Earth Sci. 88, 230–245.
- Faure, M., Lu, C.-Y., Chu, H.-T., 1991. Ductile deformation and Miocene nappe-stacking in Taiwan related to motion of the Philippine sea plate. Tectonophysics 198, 95–105.
- Fisher, D., Willett, S., Yeh, E.-C., Clark, B., 2007. Cleavage fronts and fans as reflections of orogen stress and kinematics in Taiwan. Geology 35, 65–68.
- Ho, C.S., 1986. A synthesis of the geologic evolution of Taiwan. Tectonophysics 125,
- Ho, C.S., 1988. An Introduction to the Geology of Taiwan–Explanatory Text of the Geologic Map of Taiwan, Second Edition. Ministry of Economic Affairs, Taipei, Taiwan, Republic of China.
- Hsieh, H.-H., Yen, H.-Y., 2016. Three-dimensional density structures of Taiwan and tectonic implications based on the analysis of gravity data. J. Asian Earth Sci. 124, 247–259
- Hsieh, H.-H., Chen, C.-H., Lin, P.-Y., Yen, H.-Y., 2014. Curie point depth from spectral analysis of magnetic data in Taiwan. J. Asian Earth Sci. 90, 26–33.
- Hsu, Y.-J., Yu, S.-B., Simons, M., Kuo, L.-C., Chen, H.-Y., 2009. Interseismic crustal deformation in the Taiwan plate boundary zone revealed by GPS observations, seismicity, and earthquake focal mechanisms. Tectonophysics 479, 4–18. https:// doi.org/10.1016/j.tecto.2008.11.016.
- Hsu, W.-H., Byrne, T.B., Ouimet, W., Lee, Y.-H., Chen, Y.-G., Soest, M.V., Hodges, K., 2016. Pleistocene onset of rapid, punctuated exhumation in the eastern central range of the Taiwan orogenic belt. Geology 44, 719–722.
- Hsu, Y.-J., Lai, Y.-R., You, R.-J., Chen, H.-Y., Teng, L.S., Tsai, Y.-C., Tang, C.-H., Su, H.-H., 2018. Detecting rock uplift across southern Taiwan mountain belt by integrated GPS and leveling data. Tectonophysics 744, 275–284.
- Hu, J.-C., Angelier, J., Lee, J.-C., Chu, H.-T., Byrne, D., 1996. Kinematics of convergence, deformation and stress distribution in the Taiwan collision area: 2-D finite-element numerical modelling. Tectonophysics 255, 243–268.
- Hu, J.-C., Hou, C.-S., Shen, L.-C., Chan, Y.-C., Chen, R.-F., Huang, C., Rau, R.-J., Chen, K. H.-H., Lin, C.-W., Huang, M.-H., Nien, P.-F., 2007. Fault activity and lateral extrusion inferred from velocity field revealed by GPS measurements in the Pingtung area of southwestern Taiwan. J. Asian Earth Sci. 31, 287–302.
- Huang, C., Byrne, T., 2014. Tectonic evolution of a major tectonostratigraphic boundary in an active accretionary wedge: an example from the Tulungwan fault, southern Taiwan. J. Struct. Geol. 69, 320–333.
- Huang, T.Y., Gung, Y.C., Kuo, B.Y., Chiao, L.Y., Chen, Y.N., 2015. Layered deformation in the Taiwan orogeny. Science 349, 720–723.
- Ide, S., Yabe, S., Tai, H.-J., Chen, K.H., 2015. Thrust-type focal mechanisms of tectonic tremors in Taiwan: evidence of subduction. Geophys. Res. Lett. 42, 3248–3256.
- Kuo-Chen, H., Wu, F., Roecker, S.W., 2012. Three-dimensional P velocity structures of the lithosphere beneath Taiwan from the analysis of TAIGER and related seismic data sets. J. Geophys. Res. 117.
- Lacombe, O., Mouthereau, F., Angelier, J., Deffontaines, B., 2001. Structural, geodetic and seismological evidence for tectonic escape in sw Taiwan. Tectonophysics 333, 323–345.
- Lai, K., Chan, Y., Wu, Y., 2012. Pattern of active fracture zones inferred from seismic clusters in the southern central range of Taiwan. In: AGU Fall Meeting Abstracts. T53B-2712.
- Lee, C.-P., Hirata, N., Huang, B.-S., Huang, W.-G., Tsai, Y.-B., 2010. Evidence of a highly attenuative aseismic zone in the active collision orogen of Taiwan. Tectonophysics 489, 128–138.
- Lee, Y.-H., Byrne, T., Wang, W.-H., Lo, W., Rau, R.-J., 2015. Simultaneous mountain building in the Taiwan orogenic belt. Geology 43, 447–450.
- Lin, C.-H., 2000. Thermal modeling of continental subduction and exhumation constrained by heat flow and seismicity in Taiwan. Tectonophysics 324, 189–201.
- Lin, C.-W., Chen, W.-S., 2016. Geologic Map of Taiwan Geological Society of Taiwan.
- Lin, M.-L., Yang, C.-N., Wang, Y., 1984. Petrotectonic study on the Yuli belt of the Tananao Schist in the Chinshuichi area, eastern Taiwan. In: Science Reports of the National Taiwan University ACTA Geologica Taiwanica, pp. 151–188.
- Lo, C.-L., Hsu, S.-K., 2005. Earthquake-induced gravitational potential energy change in the active Taiwan orogenic belt. Geophys. J. Int. 162, 169–176.
- Lu, C.-Y., Malavieille, J., 1994. Oblique convergence, indentation and rotation tectonics in the Taiwan mountain belt. Earth Planet. Sci. Lett. 121, 93–108.

Malavieille, J., Guihot, P., Costa, S., Lardeaux, J., Gardien, V., 1990. Collapse of the thickened Variscan crust in the French Massif central: Mont Pilat extensional shear zone and St. Etienne late Carboniferous basin. Tectonophysics 177, 139–149.

- McCaffrey, R., 1992. Oblique plate convergence, slip vectors, and forearc deformation. J. Geophys. Res. Solid Earth 97, 8905–8915.
- Mesalles, L., 2014. Mountain Building at a Subduction-Collision Transition Zone, Taiwan: Insights from Morphostructural Analysis and Thermochronological Dating. PhD Thesis. Université Pierre et Marie Curie-Paris VI.
- Molnar, P., Lyon-Caen, H., 1988. Some simple physical aspects of the support, structure, and evolution of mountain belts. In: Clark Jr., S.P., Burchfiel, B.C., Suppe, J. (Eds.), Processes in Continental Lithosphere. Geological Society of America Special Paper, 218, pp. 179–207.
- Molnar, P., Lyon-Caent, H., 1989. Fault plane solutions of earthquakes and active tectonics of the Tibetan Plateau and its margins. Geophys. J. Int. 99, 123–153.
- Platt, J., 2007. From orogenic hinterlands to Mediterranean-style back-arc basins: a comparative analysis. J. Geol. Soc. 164, 297–311.
- Platt, J., England, P., 1994. Convective removal of lithosphere beneath mountain beltsthermal and mechanical consequences. Am. J. Sci. 294
- Ramsey, L.A., Walker, R.T., Jackson, J., 2007. Geomorphic constraints on the active tectonics of southern Taiwan. Geophys. J. Int. 170, 1357–1372.
- Ruzgienė, B., Berteška, T., Gečyte, S., Jakubauskienė, E., Aksamitauskas, V.Č., 2015. The surface modelling based on UAV Photogrammetry and qualitative estimation. Measurement 73, 619–627.
- Seyferth, M., Henk, A., 2004. Syn-convergent exhumation and lateral extrusion in continental collision zones—insights from three-dimensional numerical models. Tectonophysics 382, 1–29.
- Stanley, R.S., Hill, A.B., Chang, H.C., Hu, H.N., 1981. A transect through the metamorphic core of the central mountains, southern Taiwan. In: Memoirs of the Geological Society of China, 4, pp. 443–473.
- Suarez, G., Molnar, P., Burchfiel, B.C., 1983. Seismicity, fault plane solutions, depth of faulting, and active tectonics of the Andes of Peru, Ecuador, and southern Columbia. J. Geophys. Res. 88 (10), 403–410, 428.
- Suppe, J., 1981. Mechanics of mountain building and metamorphism in Taiwan. In: Mem. Geol. Soc. China, 4, pp. 67-89.
- Suppe, J., 1984. Kinematics of arc-continent collision, flipping of subduction and backarc spreading near Taiwan. In: Memoirs of the Geological Society of China, 6, pp. 21–33.
- Suppe, J., Hu, C.T., Chen, Y.J., 1985. Present-day stress directions in western Taiwan inferred from borehole elongation. In: Petroleum Geology of Taiwan, 21, pp. 1–12.
- Teng, L.S., 1990. Geotectonic evolution of late Cenozoic arc-continent collision in Taiwan, Tectonophysics 183, 57–76.
- Thatcher, W., Foulger, G., Julian, B., Svarc, J., Quilty, E., Bawden, G., 1999. Present-day deformation across the Basin and range province, western United States. Science 283, 1714–1718.
- Tibaldi, A., Bonali, F.L., 2018. Contemporary recent extension and compression in the central Andes. J. Struct. Geol. 107, 73–92.
- Wang, Y.-J., Ma, K.-F., Mouthereau, F., Eberhart-Phillips, D., 2010. Three-dimensional Qp-and Qs-tomography beneath Taiwan orogenic belt: implications for tectonic and thermal structure. Geophys. J. Int. 180, 891–910.
- Wu, Y.M., Zhao, L., Chang, C.H., Hsu, Y.J., 2008. Focal-mechanism determination in Taiwan by genetic algorithm. Bull. Seismol. Soc. Am. 98, 651–661.
- Wu, J., Suppe, J., Lu, R., Kanda, R., 2016. Philippine Sea and East Asian plate tectonics since 52 Ma constrained by new subducted slab reconstruction methods. J. Geophys. Res. Solid Earth 121, 4670–4741.
- Yin, A., Kapp, P.A., Murphy, M.A., Manning, C.E., Mark Harrison, T., Grove, M., Lin, D., Xi-Guang, D., Cun-Ming, W., 1999. Significant late Neogene east-west extension in northern Tibet. Geology 27, 787–790.
- Yu, S.-B., Cheng, H.-Y., Kuo, L.-C., 1997. Velocity field of GPS stations in the Taiwan area. Tectonophysics 274, 41–59.
- Žalohar, J., 2009. T-TECTO 3.0 professional integrated software for structural analysis of fault-slip data. In: Introductory Tutorial, 56.
- Žalohar, J., Vrabec, M., 2007. Paleostress analysis of heterogeneous fault-slip data: the Gauss method. J. Struct. Geol. 29, 1798–1810.
- Zhao, M., Qiu, X., Xia, S., Xu, H., Wang, P., Wang, T.K., Lee, C.-S., Xia, K., 2010. Seismic structure in the northeastern South China sea: S-wave velocity and Vp/Vs ratios derived from three-component OBS data. Tectonophysics 480, 183–197.